applied sciences

MDPI

Article

A Study on the Effects of Hob Temperature on the Rock-Breaking Characteristics of Sandstone Strata

Yun-Gui Pan [1], You-Liang Chen [1,*], Xi Du [1], Hui-Dong Tong [1], Fei-Yu Tang [1], Xiao-Jian Wu [2], Su-Ran Wang [1], Shao-Ming Liao [3] and Bin Peng [1]

[1] Department of Civil Engineering, School of Environment and Architecture, University of Shanghai for Science and Technology, Shanghai 200093, China; panyungui1997@163.com (Y.-G.P.); duxijl@163.com (X.D.); thd123456winter@163.com (H.-D.T.); tangyufei108@163.com (F.-Y.T.); wangsuran@usst.edu.cn (S.-R.W.); pengtj77@hotmail.com (B.P.)

[2] Shanghai Construction Engineering Group Engineering Research Institute, Shanghai 201999, China; wuxiaolian@scgtc.com.cn

[3] Department of Geotechnical Engineering, College of Civil Engineering, Tongji University, 1239 Siping Road, Shanghai 200092, China; engcentatongj@edu.cn

* Correspondence: chenyouliang2001@163.com

Abstract: To explore the effect of hob temperature on the rock-breaking characteristics of full-section tunnel boring machines (TBMs) in sandstone strata, high-temperature furnace heating experiments of sandstone and physical and mechanical experiments at room temperature and high temperatures were conducted to obtain the mechanical properties of sandstone at different temperatures. The mechanical properties at different temperatures were calibrated using PFC^{3D} to obtain micro-mechanical and thermodynamic parameters and establish a rock-breaking model. The orthogonal experiments were used to establish the simulation experiments of rock breaking under different temperatures, confining pressure conditions, knife tip distances, and penetration degrees. The results show that the hob tip force is gradually increasing with an increase in the confining pressure. When below 600 °C, there is little temperature transfer from particle to particle as the temperature increases. At this time, with the two sides of the rock slag flaking, the hob knife tip force is the first to reduce. After 600 °C, with the expansion of the rock extrusion hob, the temperature rises on both sides; at this time, the hob tip force also increased. The hob tip force is minimal at a tip distance of 70 mm and an S/P of 14. As the surrounding pressure increases, the rock-breaking efficiency of the hobber decreases. The highest rock-breaking efficiency is achieved at 25 °C and 600 °C. The rock-breaking efficiency is highest when the knife tip distance is designed to be 70 mm, and when the S/P is 14. The three-dimensional constitutive analysis of rock-breaking particles showed that the increment caused by the hob temperature is mainly distributed in the normal force direction in the surrounding rock without any confining pressure, and the increment caused by the hob temperature exposed to the confining pressure occurs in all directions.

Keywords: PFC^{3D}; tunnel boring machine (TBM); temperature; numerical simulation; confining pressure

Citation: Pan, Y.-G.; Chen, Y.-L.; Du, X.; Tong, H.-D.; Tang, F.-Y.; Wu, X.-J.; Wang, S.-R.; Liao, S.-M.; Peng, B. A Study on the Effects of Hob Temperature on the Rock-Breaking Characteristics of Sandstone Strata. *Appl. Sci.* **2024**, *14*, 2258. https://doi.org/10.3390/app14062258

Academic Editor: Eugene J. OBrien

Received: 19 January 2024
Revised: 2 March 2024
Accepted: 5 March 2024
Published: 7 March 2024

1. Introduction

In the context of rapid economic development, the exploration and utilization of underground spaces are becoming more exhaustive, bringing forth a spectrum of complex challenges. One of the critical issues encountered is the wear and damage of tools during shield machine tunneling operations. A notable factor contributing to this challenge is the high temperature of the hob during rock cutting, which significantly influences the mechanical properties of the rock formation and subsequently alters the damage patterns. Considering the high costs and practical limitations of direct experimental studies to address hobbing-related problems, numerical simulation has emerged as a pivotal approach for conducting in-depth analysis and improving our understanding of these issues [1].

Extensive research has been conducted on rock destruction patterns, particularly focusing on the study of rock cracks [2,3]. One contribution in this field was made by Atkinson et al. [4], who conducted a detailed study on the fracture toughness of granite in the temperature range of 20 °C to 500 °C. Their research revealed critical insights into the fracture toughness of granite and the acoustic emission properties of the rock during the damage process under high-temperature conditions. Similarly, Lau et al. [5] embarked on conducting an in-depth study centered around the mechanical properties of rocks under the influence of low peritectic temperatures. Their work encompassed a range of properties, including Poisson's ratio, the modulus of elasticity, fracture toughness, and compressive strength. They successfully deduced the damage mechanism of rock mechanical properties as influenced by temperature variations and time. Further, Shao et al. [6] made noteworthy advancements in understanding granite's mechanical parameters at both room temperature and elevated temperatures. Their approach integrated basic mechanical testing with acoustic emission and microelectron microscopy observations, leading to a comprehensive analysis of thermal damage in rocks. Based on the mechanical parameters derived from these physical tests, they constructed a granite model and completed a numerical simulation study of thermal rupture in a state devoid of lateral stress. Another innovative approach was undertaken by AI-Shayea et al. [7], who employed the acoustic emission method to investigate the damage process of rocks under different temperature conditions. Their study provided valuable insights into the fracture characteristics of granite in the temperature range of 20 °C to 50 °C. In the realm of applying advanced computational techniques, Liu et al. [8] explored the potential of deep recurrent neural networks and convolutional neural networks for vibration-based ground recognition at mining sites. Their work represents a significant stride in applying machine learning and artificial intelligence in geological studies. Complementing these approaches, Wane et al. [9] utilized the thermodynamic coupling module in PFC^{2D} to analyze rock fracture phenomena and the pattern of crack expansion in temperatures ranging from 10 °C to 120 °C. This study provided a nuanced understanding of the thermal effects on rock fracture behavior. Ali et al. [10] ventured into the domain of microwave-induced thermal damage in mineral particles using discrete element particle flow. Their model, comprising calcite as the matrix and galena as embedded particles, underscored the crucial influence of particle size on the simulation results. This finding highlighted the necessity of carefully adjusting and calibrating parameters in particle flow software to accurately simulate and predict the behavior of mineral particles under thermal stress.

In the study of thermal effects on rock breaking, it was observed that when the thermal expansion coefficient of embedded particle galena exceeds that of matrix particle calcite, cracks extend in a direction perpendicular to the intersection of embedded and matrix particles. This phenomenon occurs irrespective of the size or shape of the embedded particles. Zhao et al. [11] utilized PFC to explore the effects of different cooling methods on the Brazilian cleavage of granite post high-temperature treatment. They constructed numerical models for particles of varying diameters, based on the distribution characteristics of fine components on the surfaces of standard disc specimens used in Brazilian splitting tests. These simulations revealed that for specimens without heat treatment, Brazilian splitting strength diminished with increasing particle size. However, below 400 °C, the compression strength remained relatively unaffected. For the same particle size, heat-treated granite exhibited decreased Brazilian splitting strength, with higher temperatures correlating to lower strength. Interestingly, the impact of two cooling methods—water and natural cooling—on the Brazilian splitting strength of granite was found to be negligible. Additionally, as particle sizes increased, the length of thermally induced cracks grew, while their number decreased.

Roxborough and Phillips [12] established that the rock-breaking load exerted by a hob is not only influenced by the projected area of the hob blade on the rock surface but also by the rock's compressive strength. This was concluded by studying the stress intensity caused by hob action when the rock's compressive strength was exceeded. Sanio et al. [13]

developed a mechanical model of rock breaking via hobbing, based on rock extrusion and tensioning mechanisms. They deduced that the spacing of hob-cutting grooves relates to the length of tension cracks and derived an equation for the normal thrust and hobbing force of disc-shaped hobbing based on zero moment of force. Cho et al. [14] conducted uniaxial compression experiments on laminated gneiss, mud slate, and schist with varying dip angles, analyzing that the uniaxial compression damage patterns in laminated rocks of different dip angles are essentially similar. Liu et al. [15] employed discrete element software to simulate the rock-breaking processes of single and double knives. Onate et al. [16] utilized the discrete element method to analyze the dynamic process of rock cutting via hobbing. Yu [17] developed a discrete element model to correlate the geometric distribution of rock joints with deformation characteristics. Gong et al. [18] used discrete element software for simulating rock breaking via hobbing and analyzed the crushing pattern of the rock exposed to hobbing. Innaurato et al. [19] investigated the influence of confining pressure conditions and rock-breaking surfaces on the rock-breaking process during hobbing, using a two-dimensional discrete element numerical simulation model.

When rocks suffer from multidirectional damage, their fundamental mechanical properties undergo significant changes. Tong et al. [20] investigated the constitutive relationship of sand by introducing the coupling of damage and consolidation stress. The coupling of stress and heat can also be considered in waste storage and in relation to the thermal effects of tunnel boring machine (TBM) cutterheads during cutting. From the comprehensive review of theoretical, experimental, and numerical simulation studies, it becomes evident that the current understanding of rock breaking via hobbing does not adequately consider the impact of hob temperature on rock-breaking characteristics. During excavation, the hob generates substantial heat, which alters the internal micro-contact dynamics of sandstone under these high-temperature conditions [6–10]. These changes significantly influence the force exerted by the hob and the resulting damage patterns in the surrounding rock. Variations in rock damage patterns during excavation directly impact excavation efficiency, with the direct penetration of cracks between hobs potentially accelerating this process. Due to the significant limitations of indoor experiments, research on the cutting characteristics of tunnel boring machine (TBM) cutters is primarily accomplished using numerical simulation methods. The above-mentioned articles conducted corresponding analyses on rock-breaking characteristics using the finite element method and the discrete element method, providing optimal cutter spacing and cutter forces accordingly. However, according to the actual cutting environment, the aforementioned papers did not address the issue of substantial heat generation during TBM cutter cutting.

Considering the influence of heat on rock mechanics, this paper employs the discrete element analysis method to study the cutting temperature of the tunnel boring machine (TBM). It investigates the effects of confining pressure, cutter spacing, and cutter penetration on rock-breaking characteristics under different cutting temperatures. Additionally, it determines the optimal cutter spacing under various cutting temperatures. Based on the distribution of cracks and contact quantities in the particle flow code (PFC), it explores the impact of different failure states on rock-breaking characteristics. Analyzing the influence of cutting temperature on rock-breaking characteristics can provide references for rock-breaking efficiency and cutter wear during excavation. Moreover, different forms of rock failure can offer corresponding conclusions on excavation efficiency.

2. Calibration of Mechanical Parameters

The indoor test used calcareous sandstone from Fujian Province, mainly composed of silicon, silica, calcium, clay, and iron oxide. Rock was processed into direct 50 mm cylindrical test blocks with heights of 100 mm. The high-temperature damage experiment is mainly realized using the high-temperature horse fee furnace, with a maximum temperature of 1200 °C. High-temperature damage was performed at 300 °C, 600 °C, and 900 °C, with a heating rate of 10 °C/min and a constant temperature of 4 h, and the mechanical parameters at high temperatures were measured. The basic mechanical parameters at

normal temperatures are also presented in the paper. The elastic modulus of sandstone at room temperature was 26.4 GPa, the uniaxial compressive strength was 58.72 MPa and the internal friction angle was 51.14 °C.

Su et al. [21] showed that when the ratio of model height to mean particle radius $L/R \geq 125$, the particle size does not affect the macroscopic parameters. Zhou et al. [22] showed that when (L/Rmin) [1/(1 + Rmax/Rmin)] ≥ 10, the size and number of particles have less influence on the macroscopic mechanical parameters of the model, where L is the minimum scale of the model and Rmin and Rmax are the minimum and maximum diameters, respectively. Potyondy et al. [23] suggested that Rmax/Rmin = 1.66 without considering the gradation, suggesting that the generated rock is more consistent with the physical properties of the rock. In the indoor experiment, the drill core sandstone sample with a diameter of 50 mm and a height of 100 mm is used. Therefore, according to the indoor experimental sample size, the numerical simulation model is established as a cylindrical sample with a diameter of 50 mm and a height of 100 mm. According to the influence of size effect, the minimum particle diameter is 1 mm and the maximum particle diameter is 1.66 mm. The numerical simulation model of uniaxial compression adopts the rigid wall in the PFC as the loading plate. The arrow is the loading direction and the loading ends when the test block is broken. The conventional three-axis compression numerical simulation model adopts the upper and lower walls and the cylindrical wall shape loading. The cylindrical wall controls the surrounding pressure through the servo and loads the upper and lower wall speeds until the test block is destroyed and the loading is completed. The loading diagram is shown in Figure 1 below.

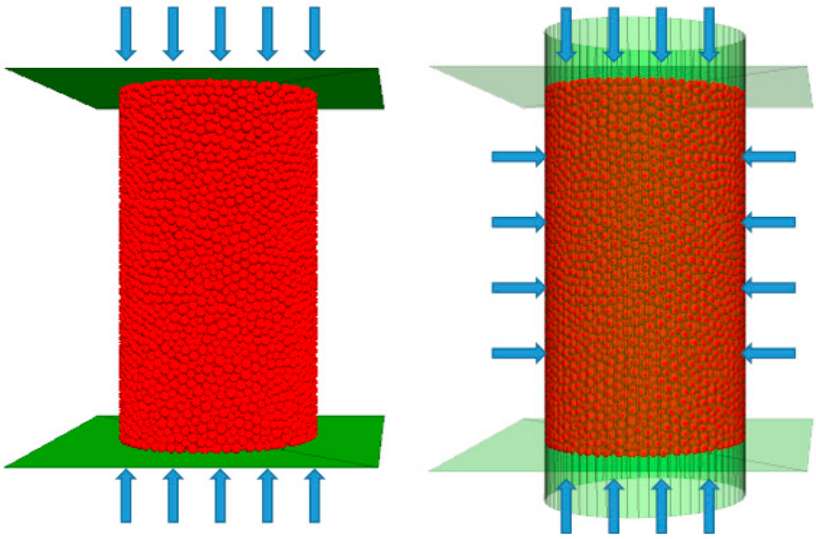

Figure 1. Numerical simulation of uniaxial compression and triaxial numerical simulation experiment.

Liu et al. [24] chose the elastic modulus E, Poisson's ratio ν, and uniaxial compressive strength *UCS* to calibrate the model's fine-scaled parameters and then performed numerical analysis. Chen et al. [25] pointed out that the model obtained using only these parameters as calibration indices cannot be used for the properties of rocks in a multidirectional stress state. Therefore, this paper considers these indicators on top of the strength indicators c and φ in the enclosing pressure state. For cracking parameters, Su et al. [21] proposed that the strength variation coefficient R_{sd} has a significant effect on the cracking strength of rocks. So, in this paper, the strength distribution is taken to obey the Gaussian distribution, which in turn is used to calibrate the cracking strength of rocks. As for rock composition, Zhang et al. [26] responded to the denseness of rock composition by varying the coefficient of the adhesion ratio θ_b. Therefore, the microscopic coefficients were selected as E_p, k_p, μ_p, σ_p, C_p, φ_p, R_{sd}, and θ_b. As shown in Figure 2, by comparing the indoor experiment and numerical simulation images, the numerical simulated stress and strain map, calibrated

according to the macroscopic mechanical parameters, is basically consistent with the experimental data map. As shown in Table 1, the elastic modulus error in the uniaxial numerical simulation is 0.03% and the uniaxial compressive strength error is 1.6%, all meeting the error permission. As shown in Figure 3, by comparing the indoor experiment and numerical simulation images, we found that the numerical simulation calibrated by the macroscopic mechanical parameters is basically consistent with the experimental data map. Table 1 shows that the error of the internal friction angle of the conventional three-axis numerical simulation is 1.70%, allowing it to meet the error permission.

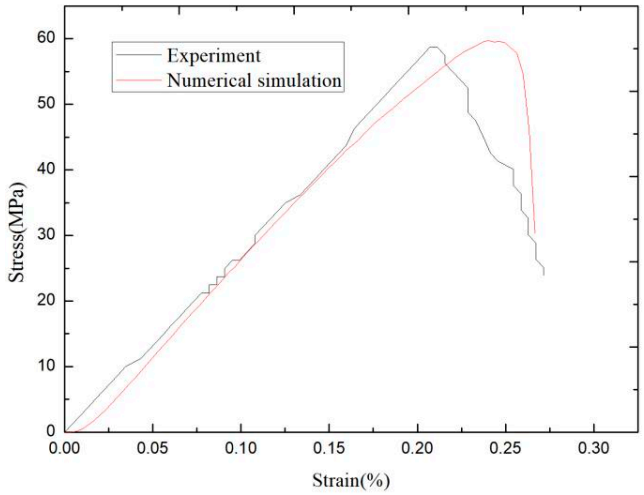

Figure 2. Numerical simulation of uniaxial compression.

Table 1. Calibration of macroscopic physical parameters of sandstone.

Macro-Parameter	*E* (GPa)	*UCS* (MPa)	*Φ* (°)
value	26.64	58.72	51.14
Initial determination	26.63	59.69	52.14
Error	0.03%	1.60%	1.70%

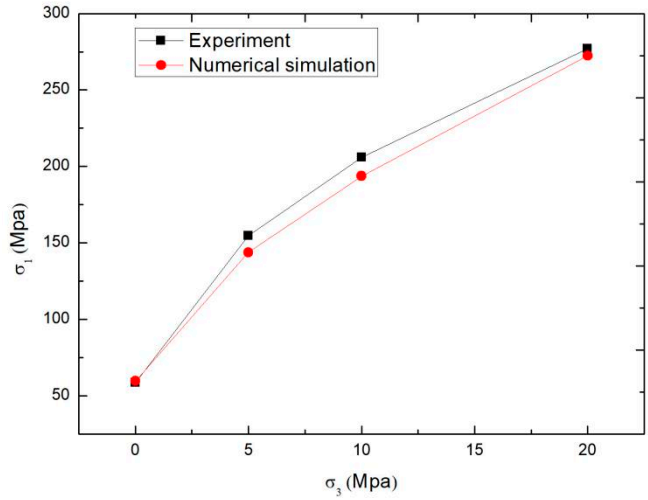

Figure 3. Numerical simulation of the triaxial experiment.

First, a suitable θ_b was selected according to the denseness of the sandstone, and the elastic modulus was calibrated by adjusting E_p, Poisson's ratio was calibrated by adjusting k_p, compressive strength was calibrated by adjusting C_p and σ_p, the internal friction

angle was calibrated by adjusting φ_p and μ_p, and the cracking strength was calibrated by adjusting R_{sd}. The final calibration results are shown in Table 1 below, and we found that the errors of the macroscopic parameters are within 5%. The values of the relevant microscopic parameters are shown in Table 2.

Table 2. Initial determination of microscopic parameters.

Micro-Parameter	E_p (GPa)	μ_p	k_p	C_p (MPa)	σ_p (MPa)	φ_p (°)	R_{sd}	θ_b
value	1.20	0.97	1	16.64	8.32	75	0.42	0.7

By comparing the failure modes of indoor experiments and numerical simulation experiments, we found that the calibrated numerical simulation model is basically the same in terms of crack development, as well as in terms of the failure mode, showing through-crack failure in oblique sections. The specific failure mode diagram is shown in Figure 4 below.

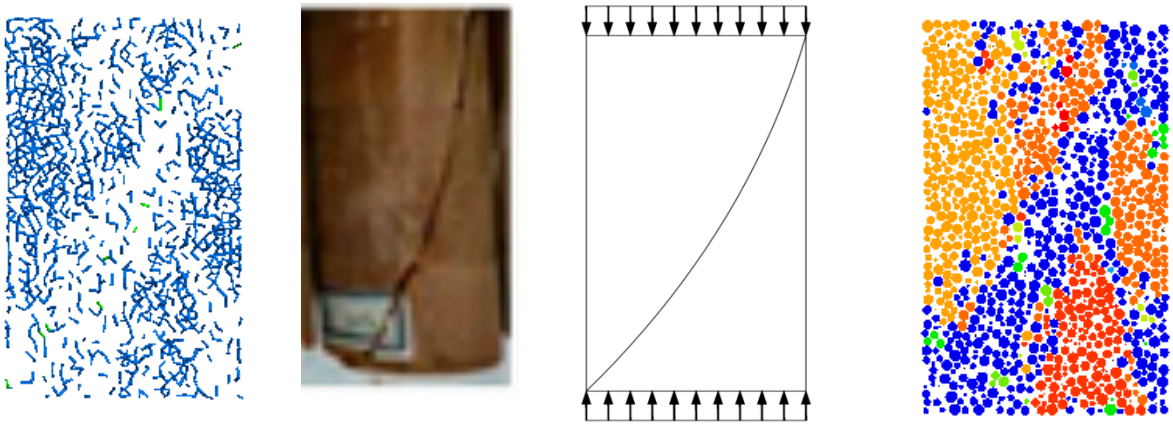

Figure 4. Triaxial numerical simulation experiment.

As shown in Figures 5 and 6, from the numerical simulation analysis of three-dimensional grouping analysis, it is clear that the sandstone shows an overall distribution of contact numbers along the circumference before loading. After loading, the specimen as a whole undergoes penetration damage along the intermediate cracks due to the generation of intermediate assertive tensile cracks, and the circumferential particle contact bonds break and decrease sharply so that the contact number presents a tight up-and-down distribution, which is consistent with the damage simulation of indoor experiments. It can be seen from the contact forces that the member shows a damage pattern with concentrated forces around it due to the generation of the main crack in the middle. Furthermore, with the increase in temperature, the loss rate of sandstone gradually rises. In indoor experiments, this is manifested by the shedding of granular particles with a powdery appearance on the surface. In numerical simulations, it is reflected in the PFC particles' contact bonds reaching the fracture strength, leading to failure. This phenomenon is related to the composition of the rock. In sandstone, the clay components, under the influence of high temperatures, detach from the larger silica particles, subsequently detaching from the surface layer of the rock mass. At around 300 °C, the clay minerals undergo expansion, causing the rock mass to undergo a compacted state. However, with the continued increase in temperature, the rock mass develops penetrating cracks. At this point, internal pores gradually enlarge, which is the reason for the increase in particle porosity in the central part, as shown in Figure 4.

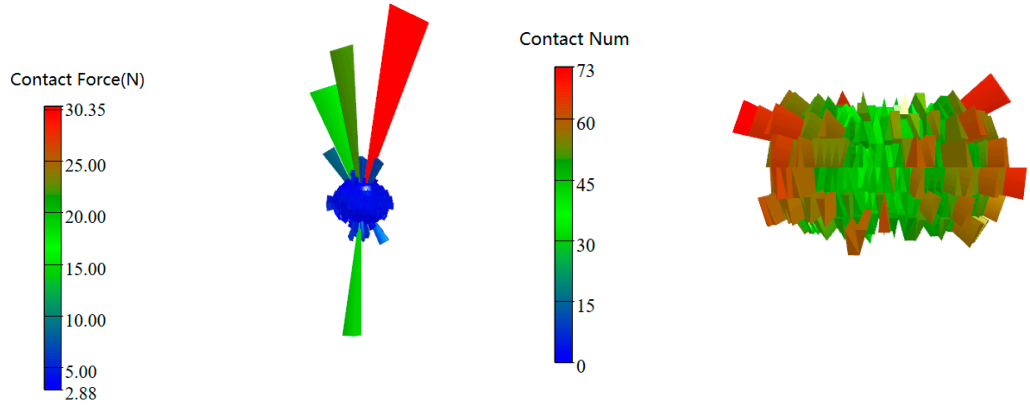

Figure 5. Contact force distribution before loading and contact number distribution group composition.

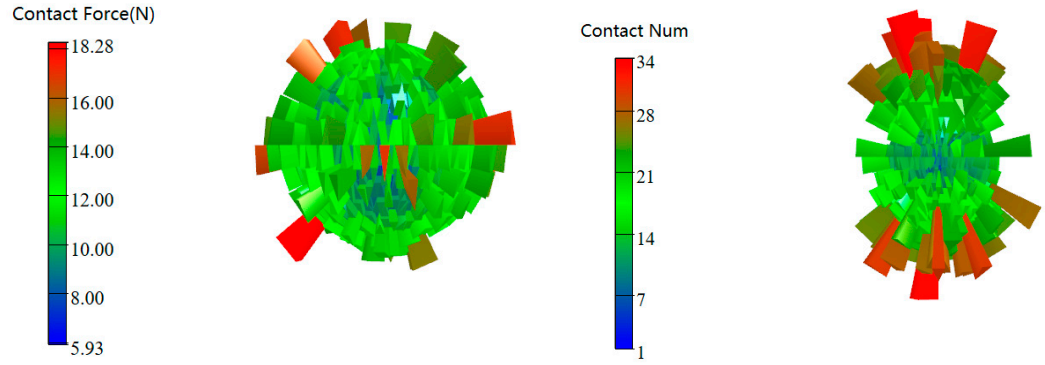

Figure 6. Contact force distribution after loading and contact number distribution group composition.

3. Calibration of Thermodynamic Parameters

Thermodynamic modeling was performed based on the model after the previous calibration of the basic mechanical parameters. Contact was made using a thermoanalytical contact model (thermopile), which is based on Fourier's law of heat conduction and defines the relationship between the continuum heat flux vector and the temperature gradient. See Equations (1) and (2) below.

$$-\frac{\partial q_i}{\partial x_i} + q_v = \rho C_v \frac{\partial T}{\partial t} \tag{1}$$

$$q_i = -k_{ij} \frac{\partial T}{\partial x_i} \tag{2}$$

PFC^{3D} generates thermal strain by considering the thermal expansion of the particles, and the linear parallel bonding model can consider the thermal expansion of the bonding bonds, acting on the following relationship. See Equations (3) and (4) below.

$$\Delta \mathrm{R} = \alpha \mathrm{R} \Delta \mathrm{T} \tag{3}$$

$$\Delta \overline{\mathrm{F_n}} = -\overline{k_n} \mathrm{A} (\overline{\alpha} \overline{\mathrm{L}} \Delta \mathrm{T}) \tag{4}$$

where α is the linear expansion coefficient, R is the particle radius, ΔT is the temperature increment, ΔR is the particle radius increment, $\overline{k_n}$ is the normal bond stiffness, A is the cross-sectional area of the adjacent particle bond, $\overline{\alpha}$ is the linear expansion coefficient of the bonding material, $\overline{L}$ is the bond length, and ΔT is the temperature increment.

The following numerical simulation model was established according to the selected thermodynamic contact model, in which the wall around the wall and the wall above and below turned off the servo and used only as heat sources to heat the sandstone. At the same time, the indoor experiment used a high-temperature hot stove to heat the specimen. The temperature imposition model is shown in Figure 7.

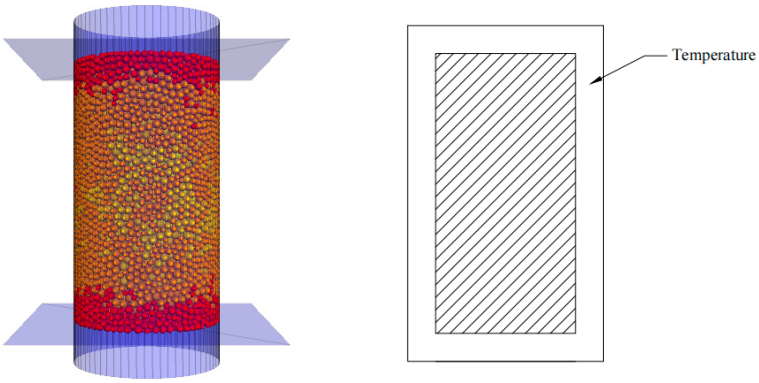

Figure 7. Temperature application model.

By turning on the thermal calculation and turning off the force calculation during the heating process, we could obtain the following temperature transfer diagram showing the heated particles. See Figure 8 below.

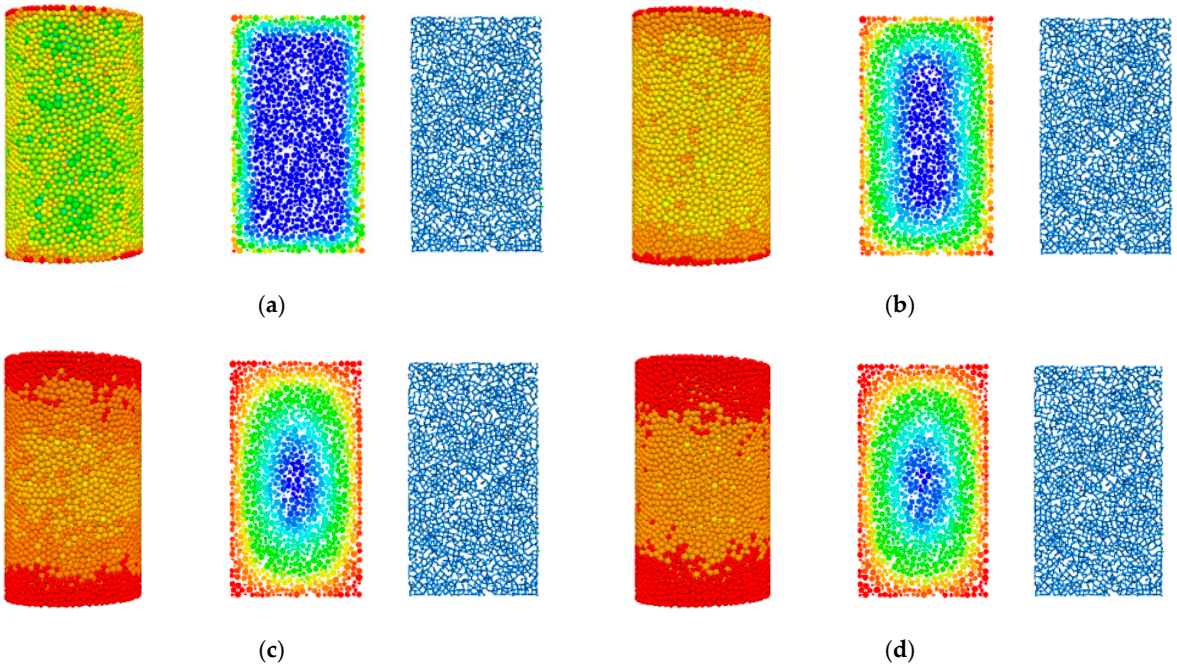

Figure 8. Temperature transfer model. (**a**) Heating 500 times. (**b**) Heating 1000 times. (**c**) Heating 2000 times. (**d**) Heating 3000 times.

The calibration errors of the internal friction angle and compressive strength are shown in Tables 3 and 4. After thermal damage was performed, uniaxial and triaxial numerical simulations were performed, and the principles of the numerical simulations were consistent with those established at room temperature. Since this contact only considers heat transfer, the amount of damage to the peak strength at 900 °C was found to be smaller than that of the test conditions. By comparing the numerical simulations with the indoor experiments, we found that the numerical simulations are basically consistent with the indoor experiments and that the error rate of peak intensity is within five percent. A comparison between laboratory experiments and numerical simulation experiments is shown in Figure 9. Since the damage to the elastic modulus was not considered in the PFC^{3D} numerical simulation, the elastic modulus of the rock masses was damaged in the actual indoor experiments due to the effects of heat. Therefore, the strain values of indoor experiments and numerical simulations under high-temperature conditions are different.

Still, since the subsequent numerical simulations study the transfer between contact forces of particles, the thermal contact model chosen for PFC^{3D} was found to be feasible. A final determination of the thermodynamic parameters is shown in Table 5. From indoor experiments, it was observed that during heating, some rock debris falls off the surface of the rock sample and partial micro-cracks appear. According to numerical simulations, it can be observed that as the temperature propagates inward, the contact bonds between PFC particles first fracture at the locations where the external contact forces are weaker. Moreover, with increasing temperature, the contact forces between particles fail, leading to the detachment of fractured particles. This phenomenon is consistent with the shedding of rock debris observed in indoor experiments. The changes in contact bonds are clearly evident in the numerical simulation results.

Table 3. Calibration results of internal friction angles.

Temperature	Laboratory Test Value	Numerical Simulation Value	Error (%)
25	52.14	51.13	1.98
300	52.69	52.26	0.82
600	51.34	53.06	3.34
900	49.84	53.83	8.00

Table 4. Calibration results of compressive strength.

Temperature	Laboratory Test Value	Numerical Simulation Value	Error (%)
25	58.72	59.70	0.017
300	57.30	57.52	0.004
600	53.56	53.79	0.004
900	46.09	48.79	0.059

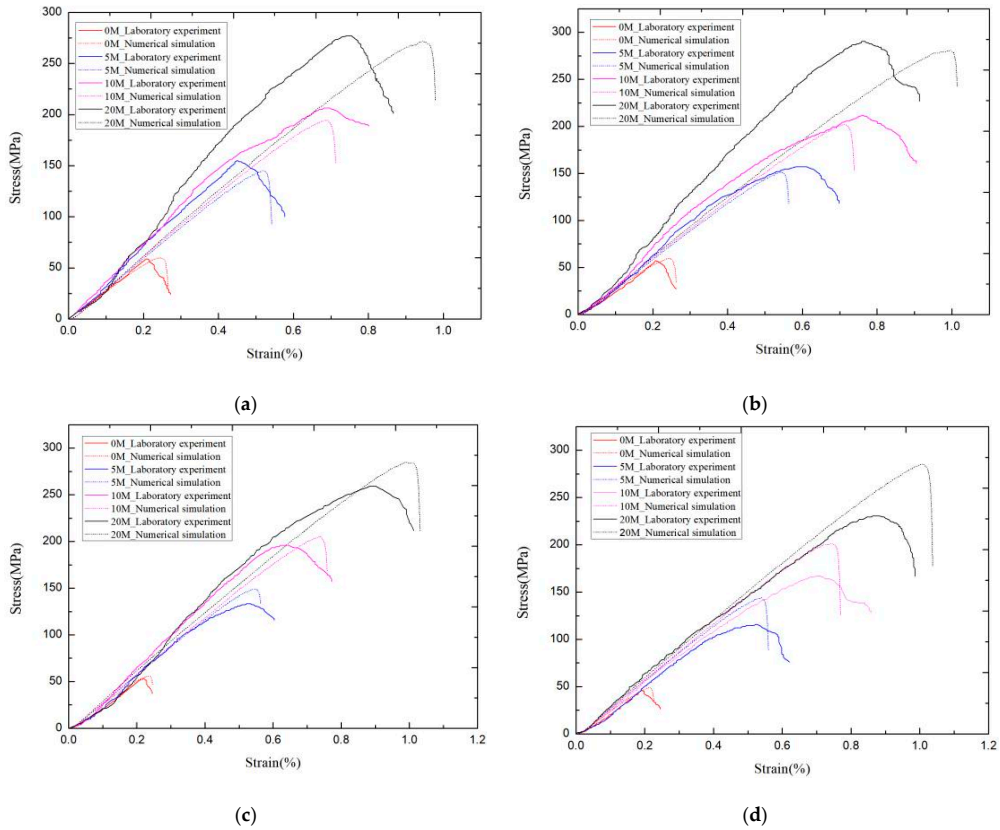

Figure 9. *Cont.*

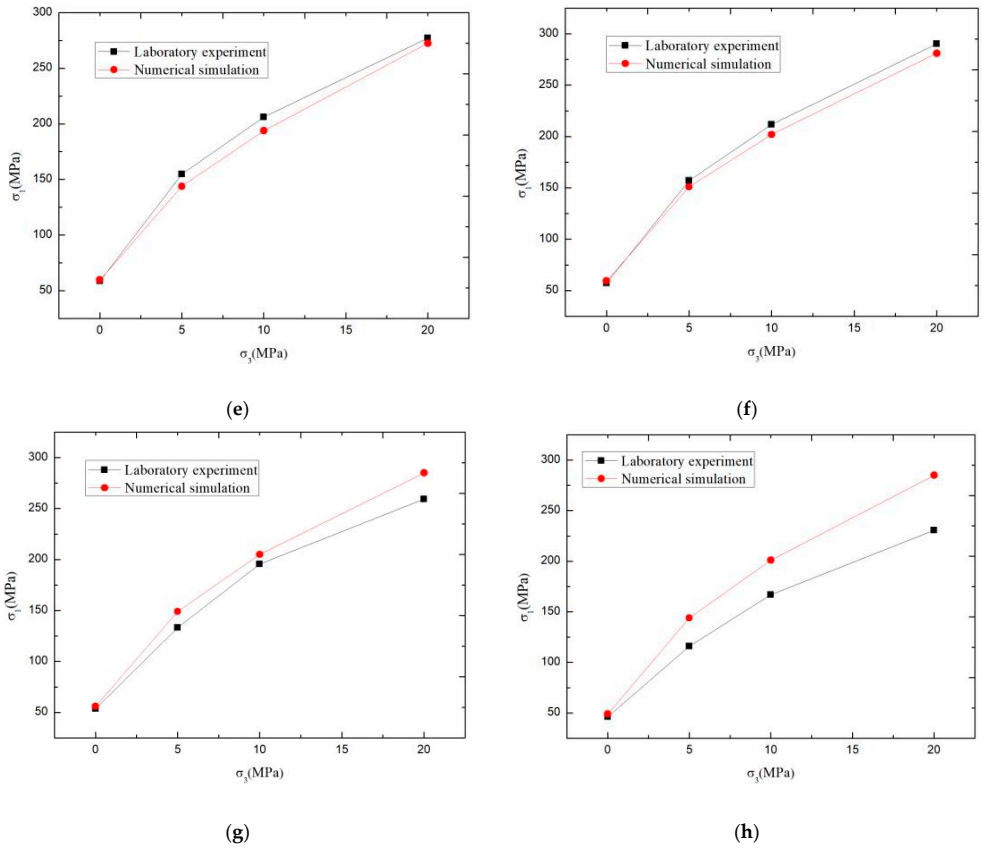

Figure 9. Comparison of numerical simulation and laboratory experiments at different sandstone temperatures. (**a**) Stress–strain diagram at 25 °C. (**b**) Stress–strain diagram at 300 °C. (**c**) Stress–strain diagram at 600 °C. (**d**) Stress–strain diagram at 900 °C. (**e**) Relationship of σ_1 and σ_3 at 25 °C. (**f**) Relationship of σ_1 and σ_3 at 300 °C. (**g**) Stress–strain diagram at 600 °C. (**h**) Relationship of σ_1 and σ_3 at 900 °C.

Table 5. Initial determination of microscopic thermodynamic parameters.

Micro-Parameter	Thermal Resistance	Coefficient of Linear Expansion	Specific Heat
value	1.367×10^6	5.6×10^{-6}	1015

As shown in Figure 10, by comparing the contact force and contact number distribution plots at different temperatures, we found that at a temperature of 300 °C, the cracks produced by the specimen under the temperature alone break the contact bonds of the particles in the weaker parts of the contact and the number of contacts decreases for the first time. Because it is heated around, the temperature of the outermost particles rises the fastest and is the first to reach the fracture strength. As the temperature increases, the maximum contact force of the particles keeps increasing from 30.12 N to 70.69 N. The temperature of the particles in the outer ring of the specimen gradually transfers inward, and the particles inside the specimen also reach the fracture temperature. Then, the contact fracture is destroyed and the number of contacts decreases rapidly. This is consistent with the phenomenon of tiny rupture of the outer layer after heating in indoor experiments.

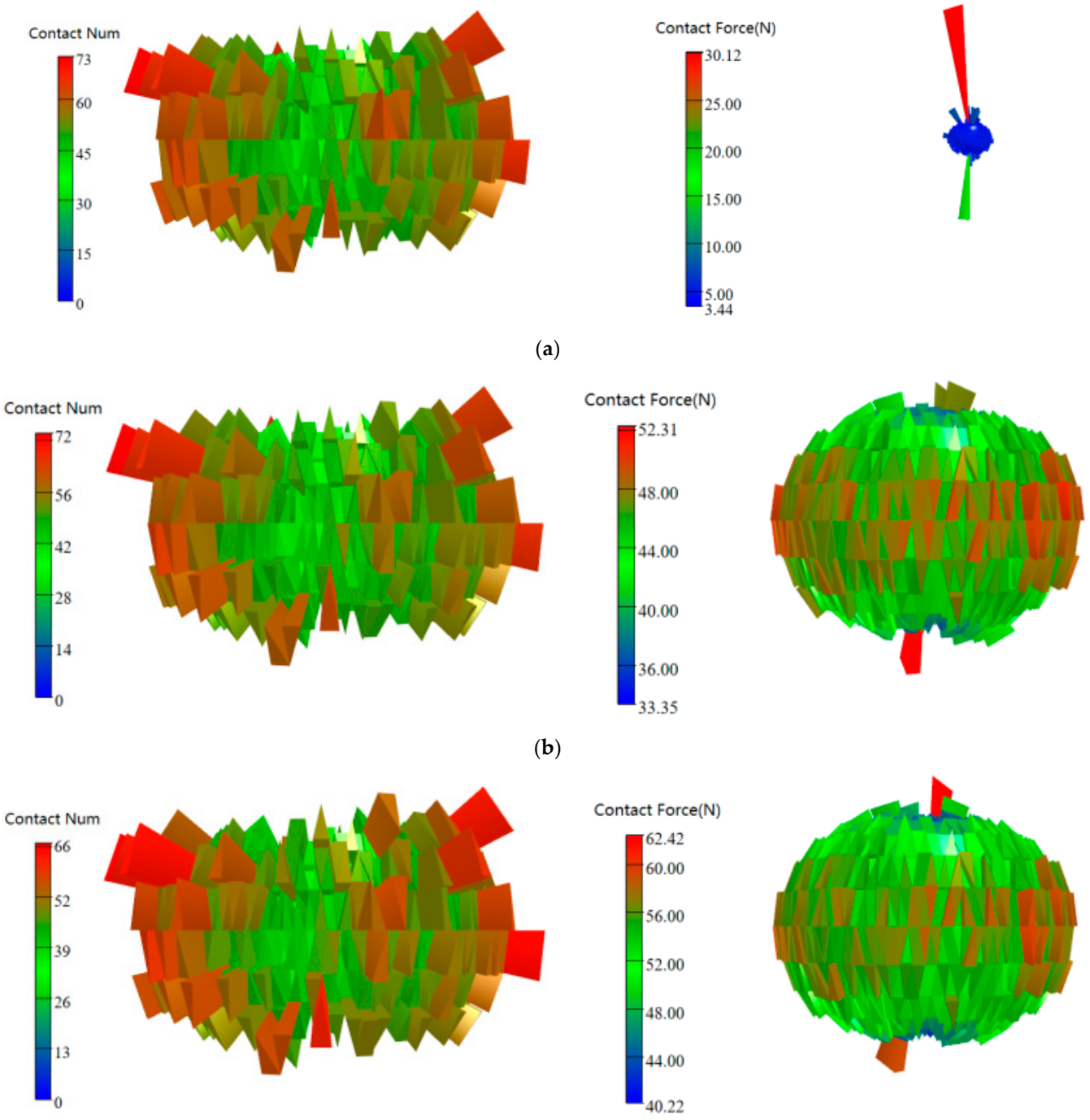

Figure 10. *Cont*.

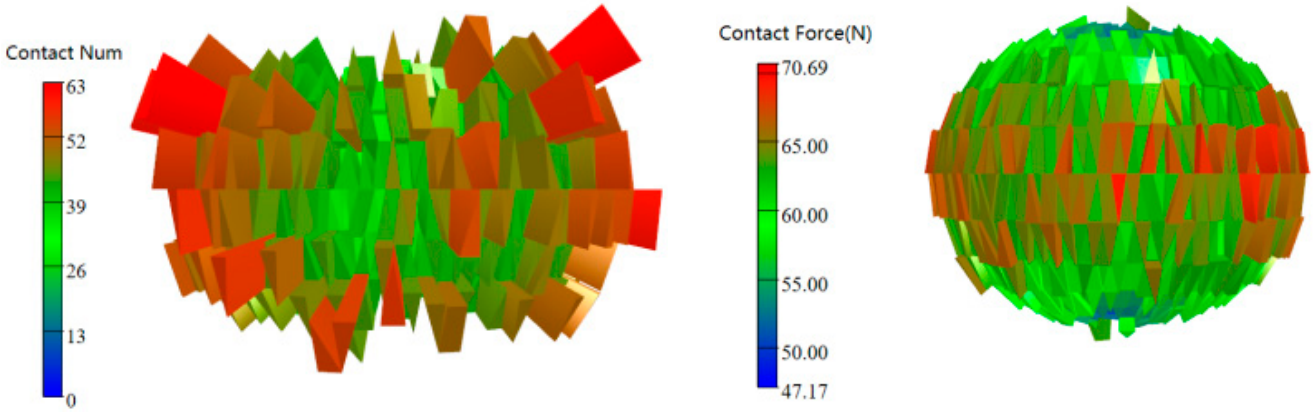

(**d**)

Figure 10. Distribution of contact force and number of contacts at different temperatures. (**a**) Number of contacts and contact forces at 25 °C. (**b**) Number of contacts and contact forces at 300 °C. (**c**) Number of contacts and contact forces at 600 °C. (**d**) Number of contacts and contact forces at 900 °C.

4. The Establishment and Analysis of the Rock Breaking Model of Hobbing

The primary contact parameters of the PFC^{3D} particles were obtained by calibrating the basic mechanical experiments obtained from the previous physical experiments, as well as by exploring the effects of heat on thermodynamic experiments. The numerical modeling of the hob was carried out to study the influence of heat on the rock-breaking characteristics during the rock-breaking process. A 17-inch Robbins hob was used for the hob, and the three-dimensional model of the hob is shown in Figure 11 below. The outer ring height of the hob was 432 mm. The hob tip thickness was 20 mm and the total width of the hob was 80 mm. The hob was generated using the wall command of PFC^{3D} based on the geometry and was imported into the model.

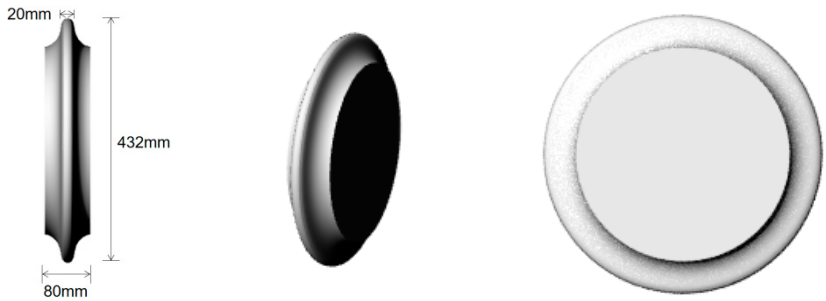

Figure 11. Diagram of the 17-inch Robbins hobber.

A rigid wall was used as the boundary and the rock enclosure pressure was added to the surrounding wall. The rock-breaking model had a radius of 1 m and a thickness of 0.5 m. The implementation steps of the rock-breaking model are as follows. (1) Sandstone rock samples are generated inside the wall, according to the porosity. (2) Then, a FISH statement is given to apply the surrounding pressure and to give the previously calibrated mechanical parameters. (3) The particles are given calibrated thermodynamic parameters and the hob tip temperatures are set to 25 °C, 300 °C, 600 °C, and 900 °C, respectively. When the particles are in contact with the hob, the temperature is transferred from the hob to the particles, and the combined effect of the hob tip force and temperature damages the particles. The hob arrangement is shown in Figure 12.

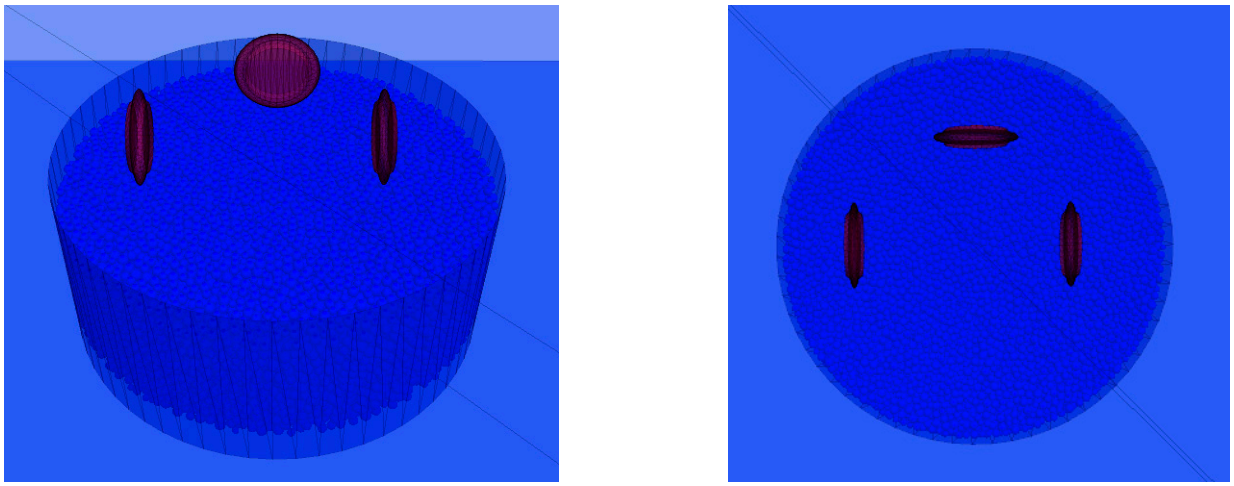

Figure 12. Hob arrangement diagram.

Because there are too many variable factors to study the rock-breaking effect, the following orthogonal experiments were established using orthogonal experiments to study the effects of heat, penetration (P), spacing (S), and surrounding pressure on rock breaking via hobbing. The details are shown in Table 6. Rock-breaking efficiency is determined by specific energy (SE); the larger the SE of the broken knife to break the rock, the greater the energy required and the poorer the rock breaking efficiency. Specific energy is mainly determined based on mean normal force (MNF), mean torque (MT), the angle of roll θ, and the depth of penetration h. For the whole cutter, SE [27] can be expressed, as shown in Equation (5).

$$\mathrm{SE} = \frac{\mathrm{HF}\cos(\frac{\phi}{2})\sum_{i=1}^{n} S_i^{\frac{1}{3}} + 2\pi \mathrm{F}\sin(\frac{\phi}{2})\sum_{i=1}^{n} S_i^{\frac{1}{3}}\sum_{\frac{1}{3}}^{\mathrm{k}} S_i}{\pi R_t^2 h} \quad (5)$$

Table 6. Orthogonal experiment table.

Number	Temperature T (°C)	P (mm)	S (mm)	Confining Pressure, (MPa)	Mean Normal Force, MNF (KN)	Specific Energy, SE (MJ/m^3)
1	25.0	4.0	60.0	0.0	198.1	24.14
2	25.0	5.0	70.0	5.0	303.7	27.13
3	25.0	6.0	80.0	10.0	503.3	43.35
4	25.0	7.0	90.0	20.0	751.7	49.66
5	300.0	4.0	60.0	10.0	455.9	57.50
6	300.0	5.0	70.0	20.0	586.8	45.29
7	300.0	6.0	80.0	0.0	240.8	22.46
8	300.0	7.0	90.0	5.0	407.9	32.83
9	600.0	4.0	60.0	20.0	580.9	58.28
10	600.0	5.0	70.0	10.0	376.9	32.15
11	600.0	6.0	80.0	5.0	377.9	31.57
12	600.0	7.0	90.0	0.0	252.2	21.11
13	900.0	4.0	60.0	5.0	325.5	41.52
14	900.0	5.0	70.0	0.0	215.8	22.00
15	900.0	6.0	80.0	20.0	721.4	52.00
16	900.0	7.0	90.0	10.0	518.8	36.94

Multi-factor regression statistics analyzed the results of the orthogonal experimental data, and the mean of the orthogonal experimental data was taken in Figure 13 below. It can be seen from the figure that under the combined effect of heat and confining pressure, specific energy (SE) requires the largest specific energy for rock breaking at 60 mm and the lowest breaking efficiency, as well as the smallest specific energy for rock breaking at 70 mm and the highest breaking efficiency. The impact of heat on specific energy con-

sumption for rock breaking is reflected in the efficiency of rock breaking. On one hand, the increase in temperature directly leads to thermal damage on the rock at the cutting surface, resulting in fragmentation and fracture. On the other hand, the rise in temperature also causes the crushed rock debris to expand, thereby exerting pressure on the cutter. At a temperature of 600 °C, there are evident cracks on the cutting surface, and the rock debris on the cutter's cutting surface is not pressed against the cutter, resulting in optimal fragmentation efficiency. When the S/P is 14, the specific energy of rock breaking is the smallest and the rock-breaking efficiency is the highest. An increase in confining pressure will make the rock-breaking ratio increase and will make the rock-breaking efficiency decrease.

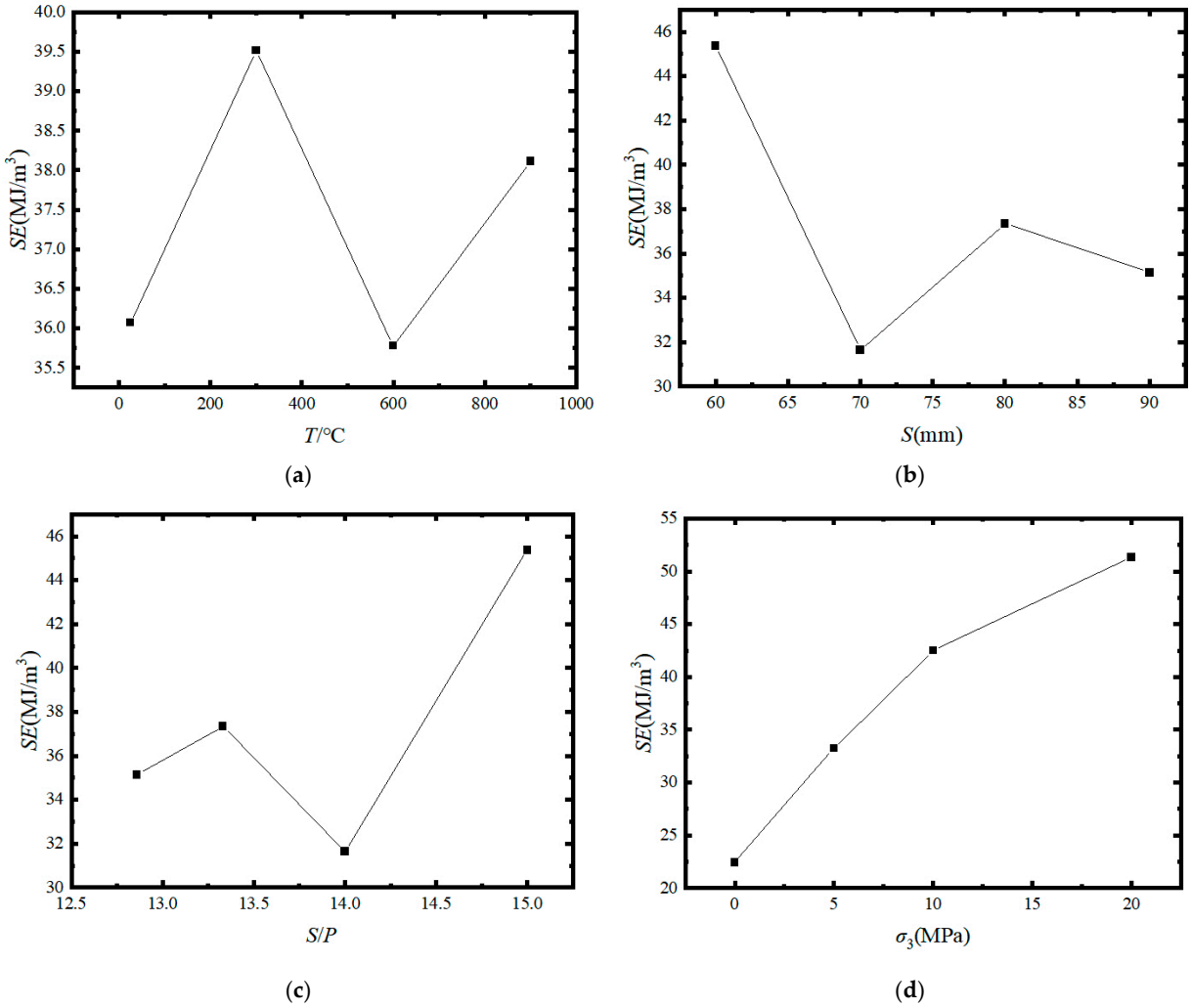

Figure 13. Specific energy (*SE*) versus penetration, tool tip distance, confining pressure, and temperature. (**a**) SE versus different temperatures. (**b**) SE versus different spacing patterns. (**c**) SE versus different penetration degrees. (**d**) SE versus different confining pressure conditions.

It can be seen from Figure 14 below that as the temperature rises, both sides of the particles with the rock-breaking process flake; at this time, the hob tip force based on the received particle contact force decreases and decreases, but after 600 °C, the tip force goes back up. This is because as the temperature continues to rise, the linear strain of the particles increases and the extrusion between the particles increases. At this time, the particles on both sides affected by the temperature will squeeze the hob, increasing the force on the hob. The effect of this phenomenon is not obvious when the temperature is low because the force of breaking rock at this time mainly comes from the horizontal and vertical dumping load of the hob, and the temperature on both sides of the spalled rock and particles is basically

not transferred over. The temperature change in the particles on both sides is not obvious and the volume deformation that occurs is low. The tip force in Figure 14 also depends on the slag formation and the fracture form. The crack forms and the cutting mouth has no obvious expansion slag, so the hob receives the minimum tip force and the lowest wear on the hob. When exposed to heat and confining pressure, and when the normal tip force is the smallest, the tip distance (S) is taken as 70 mm and the rock-breaking efficiency is also the highest under this tip distance. When exposed to heat and circumferential pressure, and when the tip force is the smallest, the tip distance/penetration (S/P) is taken as 14. The rock-breaking ratio at this tip distance is also the lowest. When exposed to heat and surrounding pressure conditions, the tool tip force increases with an increase in confining pressure, and with an increase in confining pressure, hob tilting becomes difficult. Therefore, when exposed to heat and confining pressure, the optimal knife tip distance for rock breaking with needle sandstone hobbing is 70 mm and the optimal S/P value is 14.

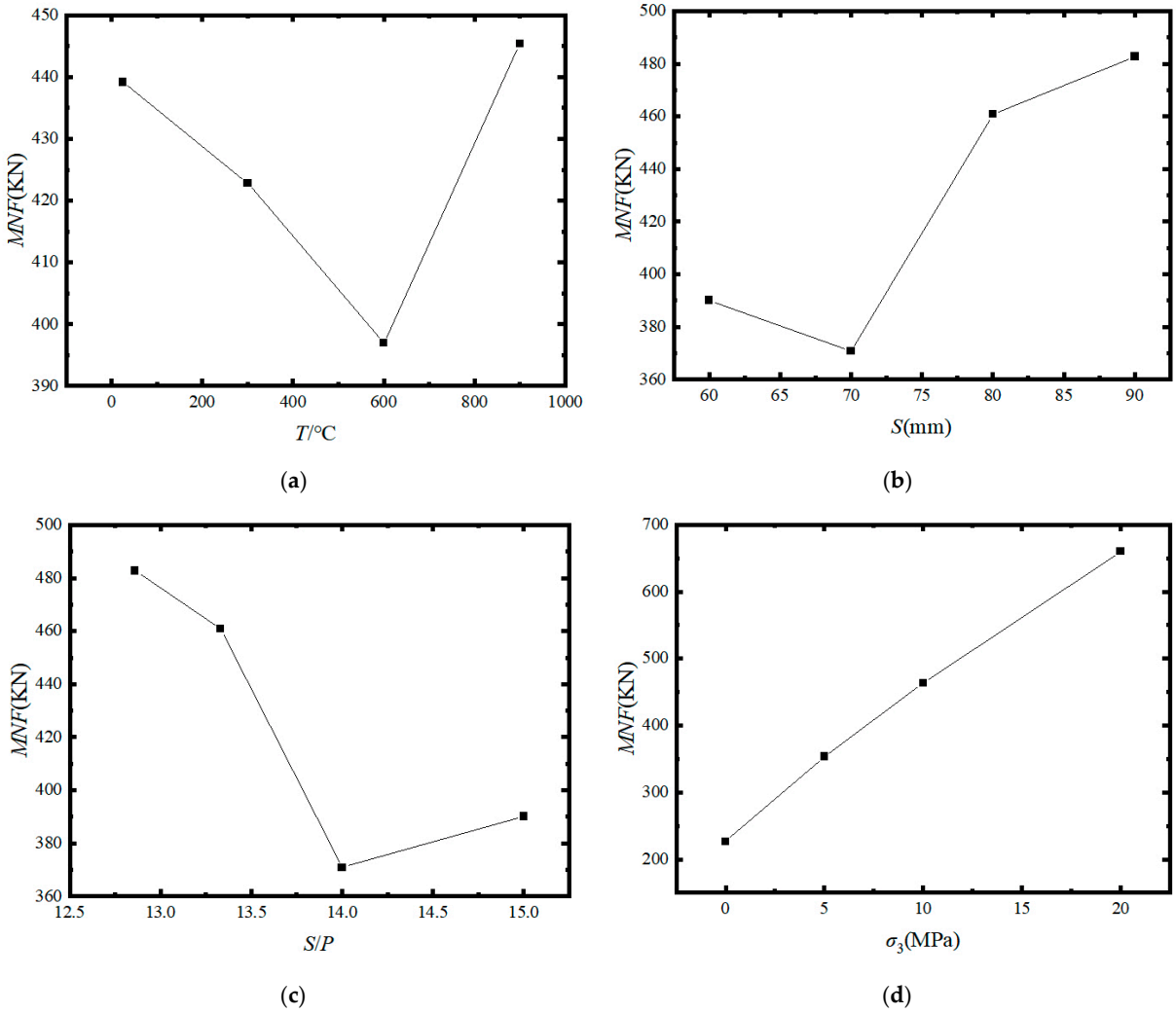

Figure 14. Mean normal force (*MNF*) versus penetration, tool tip distance, confining pressure, and temperature. (**a**) MNF versus different temperatures. (**b**) MNF versus different spacing patterns. (**c**) MNF versus different penetration degrees. (**d**) MNF versus different confining pressure conditions.

To study the reason for the force variation in the cutter from a microscopic point of view, the transverse section of the rock was taken, as shown in Figure 15. In the temperature range of 25–600 °C, with an increase in temperature, the whole fracture of the rock body develops on both sides, and the extrusion and lateral force of the cutter will gradually decrease as more and more particles flake off on both sides, which is consistent with the

conclusion of the previous analysis that the hobbing tip force decreases with the increase in temperature. However, when the temperature exceeds 600 °C, body strain occurs on both sides of the rock, the average diameter of the particles on both sides increases, and the hob tip accepts the extrusion of the particles on both sides. At this time, the extrusion force and lateral force of the tool will gradually increase, which is also consistent with the conclusion obtained earlier.

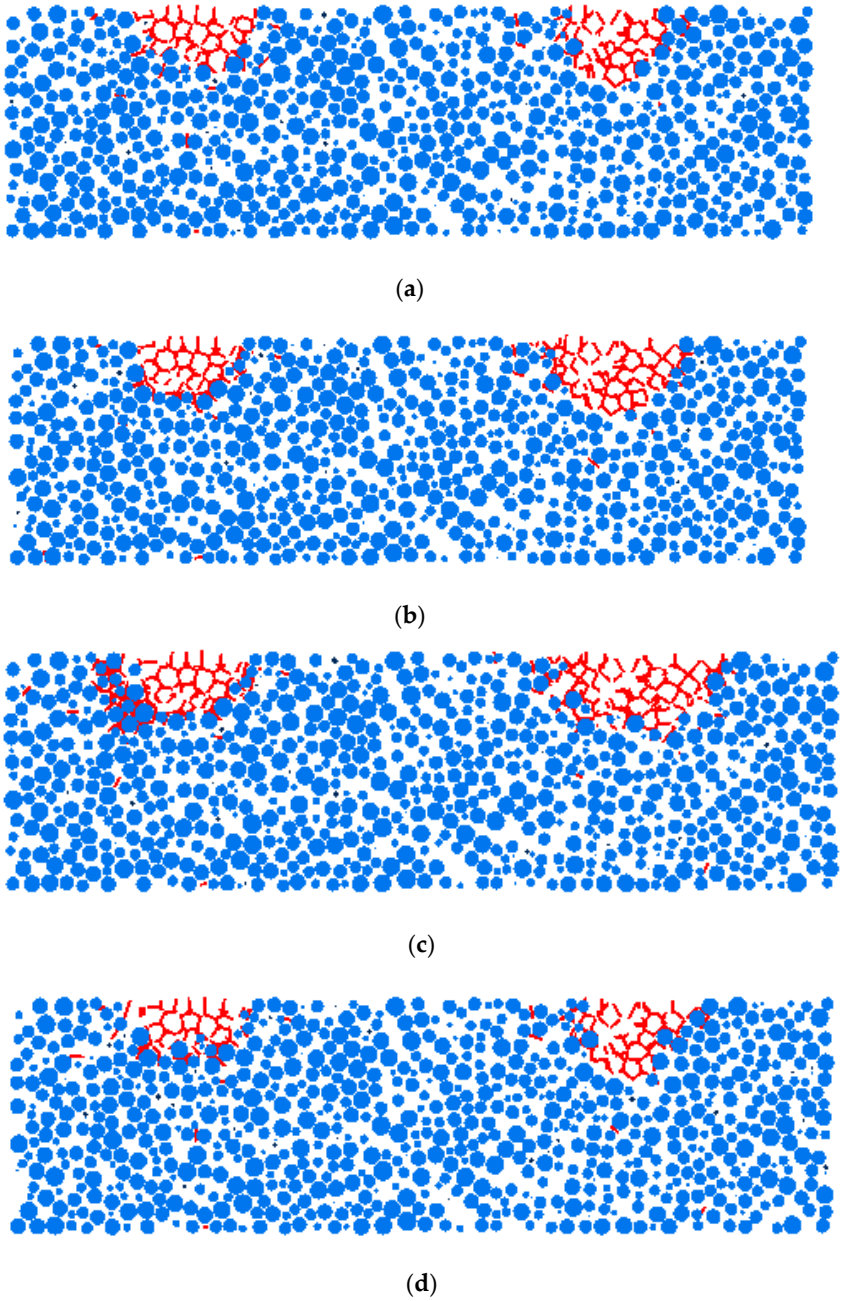

Figure 15. Diagram showing racking and crushing shapes under different temperatures: (**a**) 25 °C; (**b**) 300 °C; (**c**) 600 °C; and (**d**) 900 °C.

Rocks are often excavated in deep layers. In order to study the effect of hob temperature on the rocks of different excavation layers, the contact force of the particles after breaking the rocks was taken to make a three-dimensional group composition, and the change law of the contact force of the particles with an increase in temperature under different surrounding pressure conditions was analyzed. First of all, it can be seen from

Figure 16 that in the early stages of rock breaking, the hob temperature is too low and the contact force of the rock body at this time mainly comes from the contact of the rock body on both sides when the hob squeezes the particles. As the temperature rises, the particle contact increases due to the effects of heat, and the increased force at this time mainly comes from the temperature and the tumbling force of the hob. After 600 °C, the cracks between the hobs penetrate each other and the rock was spalled in large quantities. The contact force of the rock on both sides mainly comes from the temperature change, and the contact force increases less at this time.

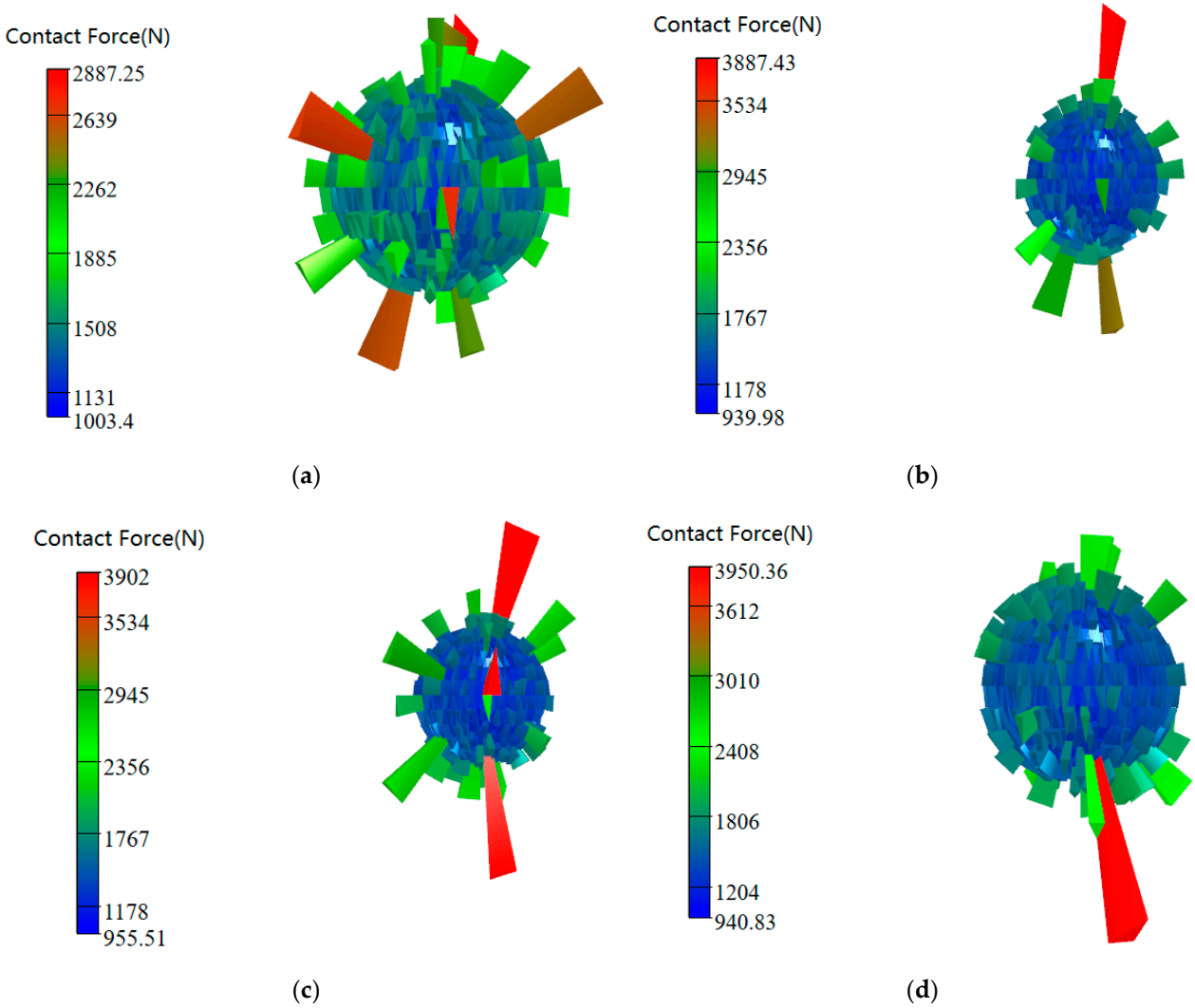

Figure 16. Variations in particle contact force with different temperatures at a confining pressure of 0 MPa: (**a**) 25 °C; (**b**) 300 °C; (**c**) 600 °C; and (**d**) 900 °C.

As shown in Figure 17, when the rock is exposed to confining pressure, in the process of breaking the rock, with an increase in temperature, the contact force of the confining rock gradually increases, without the phenomenon of first raising the block and then increasing slowly. This is because the particles will expand under the effect of heat; at this time, if there is no confining pressure effect, the rock body can be free to expand. The left and right contact before and after will not be affected by the free expansion of the particles, and the normal action of the particles mainly causes the change force at this time. However, due to the confining pressure, when the four directions are constrained, the expanding rock will be constrained and the contact force increment of the rock will be mainly affected by temperature, and the contact force will uniformly increase in each direction. In other words,

when excavating the rock body in a deep area, the hob temperature on each direction of the surrounding rock causes the force to uniformly increase in each direction.

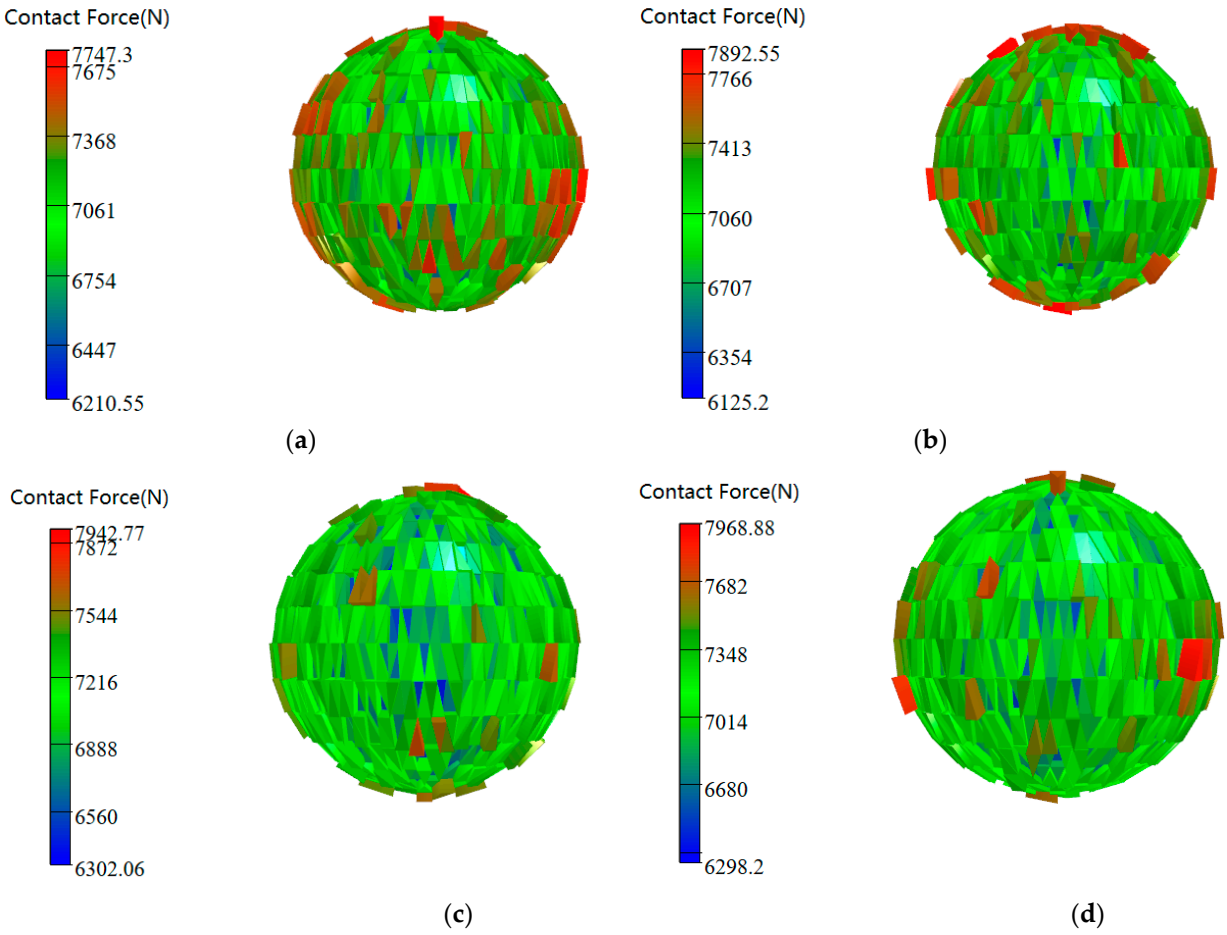

Figure 17. Variations in particle contact force with different temperatures at a confining pressure of 5 MPa: (**a**) 25 °C; (**b**) 300 °C; (**c**) 600 °C; and (**d**) 900 °C.

5. Conclusions

(1) The study determined the mechanical properties of sandstone at various temperatures through indoor experiments. Mechanical and thermodynamic parameters in PFC^{3D} were calibrated, leading to the development of a comprehensive numerical simulation of rock breaking that incorporates hob temperature. This research revealed the variation in tip force and specific energy in rock breaking under different temperature conditions, confining pressures, tip distances, and penetration depths. The analysis of crack distribution and particle arrangement showed that an increase in temperature reduces the temperature transfer between particles, initially decreasing the hob tip force due to rock flaking. As temperatures rise, the expansion of the rock body on either side of the hob results in an increase in hob tip force, which intensifies with increasing surrounding pressure conditions. When the tip range is 70 mm, the minimum tip force is 372 KN. It can be seen from Figure 14 that the tip force decreases with an increase in the tip range, and the minimum tip force is reached when the tip range is 70 mm. When the S/P value is 14, the lowest tip force is 370 KN. With an increase in S/P, the tip force first decreases and then increases, which is consistent with the changing trend of the tip distance, indicating that an optimal tip distance and an optimal S/P reduce the force on the tip, thus reducing the wear of the hob. Comparing fracture mechanisms and development in rocks under varying pressures

and temperatures indicated a more stable temperature transfer and a steady increase in contact force in rock hobs under constrained pressure conditions.

(2) The influence of the knife tip force, S/P values, and circumference pressure conditions on hob tip distances is summarized above, and the optimal S/P and S values in different cases are obtained. As can be seen from Figure 13, the specific energy of rock breaking with temperatures of 25 °C and 600 °C is minimum, and the influence of heat on rock breaking efficiency is mainly reflected in two aspects. First, the increase in temperature will make the cutting rock mass suffer heat damage and crushing. See Figure 15 for detailed microscopic damage analysis. At this time, the rock breaking efficiency increases. In addition, an increase in temperature will cause the cutting surface to expand the rock block and squeeze the hob, which will wear the hob and reduce the cutting efficiency, as shown with b and d in Figure 15.

(3) A microscopic examination of contact force variations with temperature changes in the rock surrounding the breakage site, both with and without confining pressure, was conducted. In the absence of confining pressure, increasing hob temperatures predominantly affect particles in the vertical direction, aligning with the hob's normal direction. Without constraint pressure, the circumferential force is not limited by rock expansion, making the hob's force direction predominant. Under confining pressure, however, the hobbing force increases incrementally in all directions, consistent with the temperature force.

Author Contributions: Conceptualization, X.D.; Methodology, H.-D.T.; Software, F.-Y.T.; Validation, X.-J.W.; Formal analysis, S.-R.W.; Investigation, S.-M.L.; Resources, B.P.; Writing—original draft, Y.-G.P.; Writing—review & editing, Y.-L.C. All authors have read and agreed to the published version of the manuscript.

Funding: This research was funded by "The Natural Science Foundation of Shanghai of China" (grant number 23ZR1443600) and "The National Natural Science Foundation of China" (grant number 51978401).

Institutional Review Board Statement: Not applicable.

Informed Consent Statement: Not applicable.

Data Availability Statement: The data that support the findings of this study are available from the corresponding author upon reasonable request. The data are not publicly available due to privacy.

Conflicts of Interest: Author Xiao-Jian Wu was employed by the company Shanghai Construction Engineering Group Engineering Research Institute. The remaining authors declare that the research was conducted in the absence of any commercial or financial relationships that could be construed as a potential conflict of interest.

References

1. Wang, S.; Huang, Y. Experimental study on the effect of particle size on the shear characteristics of large-displacement soil exposed to heat treatment: Shear fluctuation and heat degradation. *Eng. Geol.* **2022**, *300*, 106581. [CrossRef]
2. Liu, G.; Chen, Y.; Du, X.; Xiao, P.; Liao, S.; Azzam, R. Investigation of Microcrack Propagation and Energy Evolution in Brittle Rocks Based on the Voronoi Model. *Materials* **2021**, *14*, 2108. [CrossRef] [PubMed]
3. Liu, G.; Chen, Y.; Du, X.; Wang, S.R.; Fernandez-Steeger, T.M. Evolutionary Analysis of Heterogeneous Granite Microcracks Based on Digital Image Processing in Grain-Block Model. *Materials* **2022**, *15*, 1941. [CrossRef] [PubMed]
4. Atkinson, B.K. Mieroselsmic activity in geologic structures and materials. In *Proceedings of the 3th International Conference on AE Leighton*; Trans Tech Publications: Stafa-Zurich, Switzerland, 1984.
5. Lau, J.S.O.; Jackson, R. The effects of temperature and water saturational on mechanical properties of lacdu bonnet pinl granite. In Proceedings of the 8th International Congress on Rock Mechanics, Tokyo, Japan, 25–29 September 1995.
6. Shao, S.; Ranjith, P.G.; Wasantha, P.L.; Chen, B.K. Experimental and numerical studies on the mechanical behaviour of Australian Strathbogie granite at high temperatures: An application to geothermal energy. *Geothermics* **2015**, *54*, 96–108. [CrossRef]
7. AI-Shayea, N.A.; Khan, K.; Abduljauwad, S.N. Effects of confining pressure and temperature on mixed-mode (I~II) fracture toughness of a limestone rock. *Int. J. Rock Mech. Min. Sci.* **2000**, *37*, 629–643. [CrossRef]
8. Liu, M.; Liao, S.; Yang, Y.; Men, Y.; He, J.; Huang, Y. Tunnel boring machine vibration-based deep learning for the ground identification of working faces. *J. Rock Mech. Geotech. Eng.* **2021**, *13*, 1340–1357. [CrossRef]

9. Wanne, T.S.; Young, R.P. Bonded-particle modeling of thermally fractured granite. *Int. J. Rock Mech. Min. Sci.* **2008**, *45*, 789–799. [CrossRef]
10. Ali, A.Y.; Bradshaw, S.M. Bonded-particle modelling of microwave-induced damage in ore particles. *Miner. Eng.* **2010**, *23*, 780–790. [CrossRef]
11. Zhao, Z.; Liu, Z.; Pu, H.; Li, X. Effect of Thermal Treatment on Brazilian Tensile Strength of Granites with Different Grain Size Distributions. *Rock Mech. Rock Eng.* **2018**, *51*, 1293–1303. [CrossRef]
12. Roxborough, F.F.; Phillips, H.R. Rock excavation by disccutter. *Rock Mech. Min. Sci. Geomech.* **1975**, *12*, 361–366. [CrossRef]
13. Sanio, H.P. Prediction of the performance of disccutters in an isotropic rock. *Int. J. Rock Mech. Min. Sci. Geomenchanics Abtracts* **1985**, *22*, 153–161. [CrossRef]
14. Cho, J.W.; Kim, H.; Jcon, S.; Min, K.B. Deformation and strength anisotropy of Asan gneiss, Boryeong shale, and Yeoncheon schist. *Int. J. Rock Mech. Min. Sci.* **2012**, *50*, 158–169. [CrossRef]
15. Liu, H.Y.; Kou, S.Q.; Lindqvist, P.A.; Tang, C.A. Numerical simulation of the rock fragmentation process induced by indenter. *Int. J. Rock Mech. Min. Sci.* **2002**, *39*, 491–505. [CrossRef]
16. Onate, E.; Rojek, J. Combination of disrete element and finite element methods for dynamic analysis of geomechanics problems. *Comput. Methods Appl. Mech. Eng.* **2004**, *193*, 3087–3128. [CrossRef]
17. Yu, J.J.; Yosihiko, T.; Bo, L. Influence of geomechanics distribution of rock joints on deformational behavior of underground opening. *Tunneling Undergr. Space Technol.* **2006**, *21*, 485–491. [CrossRef]
18. Gong, Q.M.; Jiao, Y.Y.; Zhao, J. Numerical medeling of the effects of joint spacing on rock fragmentation by TBM cutters. *Tunneling Undergr. Spacing Technol.* **2006**, *21*, 46–55. [CrossRef]
19. Innaurato, N.I.; Oggeri, C.; Oreste, P.P.; Vinai, R. Experimental and numerical studies on Rock breaking with TBM tools under high stress confinement. *Rock Mech. Rock Eng.* **2007**, *40*, 429–451. [CrossRef]
20. Tong, H.; Chen, Y.; Du, X.; Chen, S.; Pan, Y.; Wang, S.; Peng, B.; Azzam, R.; Fernandez-Steeger, T.M. A State-Dependent Elasto-Plastic Model for Hydrate-Bearing Cemented Sand Considering Damage and Cementation Effects. *Materials* **2024**, *17*, 972. [CrossRef]
21. Su, H.; Dong, W.; Hu, B.W. *Application of Discrete Element Particle Flow in Hydraulic and Geotechnical Engineering*; Science Press: Beijing, China, 2017. (In Chinese)
22. Zhou, Y.; Wu, S.C.; Jiao, J.J. Study on meso-mechanical parameters of rock and soil based on BP neural network. *Rock Soil Mech.* **2011**, *32*, 3821–3826. (In Chinese)
23. Potyondy, D.O. A Flat-Jointed Bonded-Particle Material for Hard Rock. In Proceedings of the 46th US Rock Mechanics Symposium, Chicago, IL, USA, 24–27 June 2012.
24. Liu, F.Y.; Chen, P.Y.; Yu, H.M. Simulation of rock uniaxial compression and Brazilian splitting particle flow based on Flatjoint contact model. *J. Yangtze River Sci. Res. Inst.* **2016**, *33*, 60–65. [CrossRef]
25. Chen, P.Y.; Kong, Y.; Yu, H.M. Mesoscopic parameter calibration of rock uniaxial compression PFC(2D) model. *J. Undergr. Space Eng.* **2018**, *14*, 1240–1249.
26. Zhang, B.Y.; Zhang, C.S.; Wang, C.L. Calibration method of mesoscopic parameters for PFCD flat joint model. *J. Comput. Mech.* **2021**, *38*, 665–673. [CrossRef]
27. Ling, G.; Yu, T.B.; Fei, X.T. A method for predicting cutter head specific energy of TBM based on CSM model. *J. Northeast. Univ.* **2012**, *12*, 1766–1769. (In Chinese)